Research Article

Precipitator concentration-dependent opto-structural properties of MgO nanoparticles fabricated using natural brine

Sadegh Yousefi[1] · Behrooz Ghasemi[1]

Received: 5 January 2020 / Accepted: 30 March 2020 / Published online: 8 April 2020

Abstract
In this paper, MgO nanoparticles (MNPs) were synthesized using simple wet chemical precipitation technique from evaporative brine as Mg ions precursor. The effect of NaOH concentration on morpho-structural and optical properties of as-synthesized nanoparticles was studied. The obtained nanoparticles were characterized by X-ray Diffraction (XRD), transmission electron microscopy (TEM), field emission scanning electron microscope (FESEM), energy dispersive X-ray (EDS), fourier transform infrared spectroscopy and UV–Vis absorption spectroscopy. The obtained structural properties (from XRD analysis) indicated that MNPs had pure cubic phase, high crystallinity, and average crystallite size and were in good agreement with TEM and FESEM characteristics. Also, increasing the concentration of the precipitator resulted in reduced crystallites size (from 37.09 to 17.61 nm), nanoparticles size (from 35–88 nm to 22–75 nm), and strain value (from 1.23×10^{-3} to 0.57×10^{-3}). The optical properties of MNPs including absorption (A), transmittance (T), absorption coefficient (α), optical band gap energy (E_g), Extinction coefficient (k), and refractive index (n) were investigated using UV–Vis spectroscopy and examined in details.

Keywords Brine · MgO nanoparticles · Optical properties · UV–Vis spectroscopy · Band gap energy

1 Introduction

Among the various nanoparticles, magnesium oxide (MgO) has attracted a large interest due to its unique applications in the catalyst, remove of toxic species from wastewater, refractory products, paint, antibacterial materials, superconductor materials, plasma display panels (PDP) and other optical fields [1–3]. Different physicochemical methods have been developed such as sol–gel, chemical gas phase deposition, laser vaporization, hydrothermal, microwave enhanced precipitation, aqueous wet chemical and surfactant method, and polyol-mediated thermolysis are widely used for the synthesis of MNPs with special morpho-structural, optical properties [4]. Performed studies indicated that the morphology and characteristics (including optical, thermal, and etc.) of MNPs can be affected by the synthesis method and the process conditions such as, the reaction's temperature, precipitator agent's concentration, magnesium's concentration, type and concentration of the dispersing agent, suspension aging temperature and calcination's time and temperature [5].

In recent years, the optical properties of magnesium oxide nanostructures have found a special place among researchers and papers have been published in this field. Al-Ghamdi et al. [6] synthesized ultrafine MgO cubic face-centered nanowires with a mean diameter of 10 nm and a mean length of 18–20 μm. The UV–Vis characterization of these nanoparticles indicated a raised absorption peak in the low wavelength zone and an optical energy gap of 3.45 eV. They reported MgO nanowires with a wide band gap had good potential application in optoelectronic nanodevices such as plasma display panels. Al-Gaashani et al. [7] reported a simple method for the synthesis of MgO nanoflakes using a conventional microwave oven. They

✉ Sadegh Yousefi, s.yousefi@semnan.ac.ir | [1]Faculty of Metallurgy and Materials Science, Semnan University, Semnan, Iran.

proved that Herve and Vandamme's model is suitable for nanoflakes to develop the photo transformation of the solar cells. In a similar study, Hadia et al. [2] successfully synthesized MgO nanowires by the solvothermal route via $Mg(NO_3)_2{\cdot}6H_2O$ and NaOH. The UV–Vis spectrum for MgO nanowires indicates an increased absorption intensity in the low wavelength range and an optical energy gap of 4.51 eV obtained from the absorption spectra. Their studies have shown that Ghosh et al. model is adequate for solar cell usages. Obeid et al. [8] were prepared undoped and cobalt doped MgO nanopowders ($Mg_{1-x}Co_xO$, x = 0, 0.03, 0.06 and 0.12) using co-precipitation technique. They found that the band gap of doped MgO nanoparticles (MNPs) (until its solubility precinct) strongly indicated which Co ions had been accommodated into the MgO crystal lattice, and synthesized samples can be used in photo-catalysis application.

Although much progress has been made for synthesizing nano-scaleed MgO due to its various properties such as optical properties, the synthesis of MgO from impure precursors have not been reported. In the current study, we investigate the synthesis and the characterization of the MNPs by a simple wet chemical precipitation technique using brine as a magnesium precursor without any template or surfactant. The as-synthesized nanoparticles were analyzed using XRD, TEM, Field Emission Scanning Electron Microscope (FESEM), EDS and FTIR. Furthermore, UV–Vis absorption investigations of the synthesized nanoparticles were carried out and helped to estimate the optical band gap energy. The absorption coefficient, extinction coefficient, and refractive index of the MNPs have also been discussed in detail.

2 Experimental

2.1 Synthesis of MNPs

All chemicals in this study, such as NaOH (Merck), Ethanol (Merck), and Distilled water (DW) were used analytical reagent grade and were utilized without additional purification. Final brine of Khur Potash complex (KPC) (containing $MgCl_2$, $CaCl_2$, KCl, NaCl with concentration with 207, 507, 3, and 5 g L^{-1}) was used as magnesium precursor.

Here, we report the synthesis of MNPs by template-free chemical precipitation route, which is a simple and economical method. In the typical synthesis method, 50 cc of filtered brine was poured into a beaker. Under vigorous magnetic stirring and controlled pH (9–9.5), stoichiometric amounts of NaOH solution with a concentration of 1 mol L^{-1} (sample 1), 2 mol L^{-1} (sample 2), and 3 mol L^{-1} (sample 3) were added drop by drop into the brine. After completing the magnesium hydroxide [$Mg(OH)_2$] precipitation reaction from the brine (based on reaction 1), the white suspensions were aged at room temperature for 1 h.

$$\text{Brine (containing } MgCl_2,\ CaCl_2,\ \text{NaCl and KCl)} + \text{NaOH(aq)} \rightarrow Mg(OH)_2 \downarrow \text{(s)} + \text{Mother liquor (containing2NaCl, } CaCl_2 \text{ and KCl)} \quad (1)$$

Then the white sediments were detached from the mother liquor via vacuum filtration and were washed various times by using DW and absolute ethanol. Finally, after drying the $Mg(OH)_2$ cakes at 125 °C in an oven, the powders were calcinated at 650 °C in a furnace to obtain MNPs (reaction 2) [9].

$$Mg(OH)_2 \rightarrow MgO + H_2O \quad (2)$$

The obtained magnesium oxide nanoparticles were named MgO-1, MgO-2, and MgO-3, respectively, and were collected for subsequent characterizations.

2.2 Characterization

X-ray diffraction (XRD) analysis of MNPs was done using a D8-Brucker diffractometer with CuKα radiation at a scan rate of 0.065° s^{-1} and 2θ between 10° and 90° (λ = 1.5406 Å, 35 kV, 30 mA). The morphological studies of prepared nanoparticles were studied by field emission scanning electron microscopy (FESEM, MIRA3, TESCAN) with energy dispersive x-ray spectroscopy (EDS) operated at 15 kV and gold coating and transmission electron microscopy (TEM, LEO912-AB). FTIR spectra of as-synthesized nanoparticles were studied using the Shimadzu 8400 double-beam spectrometer via KBr pellet route in the range of 400–4000 cm^{-1}. The optical absorption spectrum of the MNPs was recorded by a UV–Vis spectrometer (Shimadzu UV-1650PC spectrophotometer) in range 200–1100 nm. For optical testing, 0.1 g/L solution of the as-synthesized samples was prepared in absolute ethanol by ultrasonic irradiation.

3 Results and discussion

3.1 Structural and morphological properties

The structural characterization of samples was carried out by XRD analysis. Figure 1 indicates the XRD patterns of the MNPs synthesized from impure precursor (brine). For all of the samples, the XRD spectra show diffraction peaks (2θ) at the angles of 36.83°, 42.85°, 62.22°, 74.55° and 78.51° that can be attributed to the (111), (200), (220), (311) and (222) planes (Miller index) of the Face Centered Cubic (FCC) structured MgO having space group of Fm-3m. Also, These

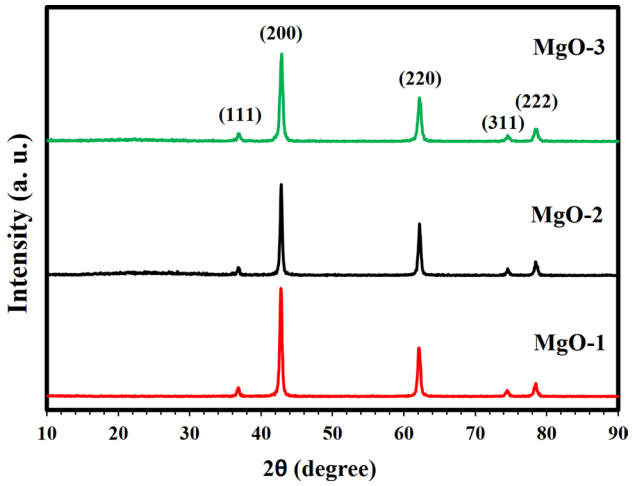

Fig. 1 XRD patterns of synthesized MgO nanopowders under different conditions

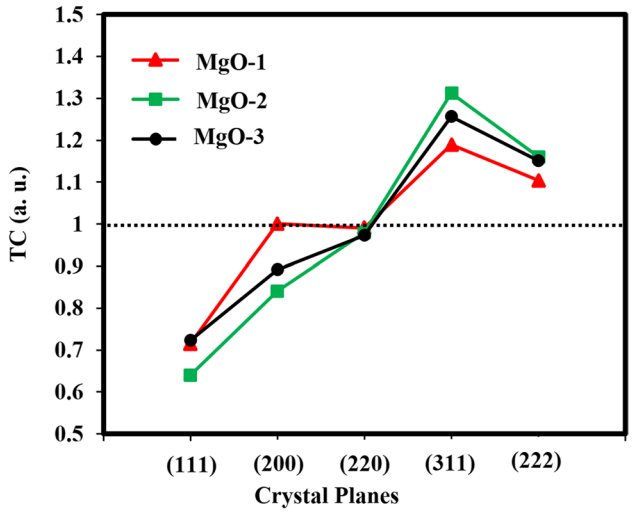

Fig. 2 The texture coefficient (TC) corresponding with crystal planes of MNPs

XRD planes are in good match with the standard JCPDS card of MgO (JCPDS 01-075-0447, a = b = c = 4.22 Å). No characteristic peaks assigned to impurities were shown, thus proving the high purity of the obtained products of the MgO NPs. Furthermore, the XRD patterns illustrate that the MgO NPs are well crystallized.

The average crystallite size (CS) of MNPs was estimated using the Scherrer's relation from the following equation [4]:

$$\mathrm{CS} = \frac{0.9\lambda}{\cos\theta\sqrt{\beta^2 - \mathrm{b}^2}} \tag{3}$$

where λ is the X-ray wavelength (1.5406 Å), β, b and θ are the FWHM of the diffraction peaks, instrumental corrected integral breadth of the reflection (Si) and diffraction angle (Bragg angle), respectively. The average crystallite size of MgO-1, MgO-2, and MgO-3 powders were estimated at about 25.29 nm, 25.66 nm 18.95 nm, respectively. As it is clear, increasing the concentration of sodium hydroxide leads to a reduction in the crystallite size of the MNPs that is due to the increase of local concentration of hydroxyl ions, supersaturation phenomenon, and prevent the growth of crystals.

The preferential orientation of the MNPs was investigated by using the texture coefficient equation (Eq. (4)) [10] and estimated results indicated in Fig. 2.

$$\mathrm{TC} = \frac{I_{(hkl)}/I_{0(hkl)}}{(1/N)\left[\Sigma_N I_{(hkl)}/I_{0(hkl)}\right]} \tag{4}$$

where I is the determined intensity of MgO samples, I_0 is the intensity of the standard card (JCPDS), and N is the count of used diffraction peaks. Any plane with a TC greater than one will be the preferred orientation for the growth of crystals. Figure 2 illustrates that in all samples, preferential orientation is along both (311) and (222) planes. Also, in the case of MgO-3 (due to increasing the concentration of NaOH), the preferential orientation has increased along these planes.

The strain derived in the synthesized materials because of crystal defects was computed by following equation [11]:

$$\varepsilon = \frac{\beta_{hkl}}{4\tan\theta} \tag{5}$$

So the strain-induced line broadening β_s is given by:

$$\beta_s = 4\varepsilon\tan\theta \tag{6}$$

Equations 3 and 5 prove that the diffraction peak width of crystallite size and strain changes as 1/cosθ and tanθ, respectively. So, the total peak broadening is obtained by summation of the portions of the crystallite size and existence strain in the synthesized powder and can be proposed as [12]:

$$\beta_{\mathrm{hkl}} = \beta_{\mathrm{D}} + \beta_{\mathrm{S}} \tag{7}$$

So:

$$\beta_{hkl} = \left(\frac{k\lambda}{D\cos\theta}\right) + 4\varepsilon\tan\theta \tag{8}$$

By rearranging above relation [10, 11]:

$$\beta_{hkl}\cos\theta = \left(\frac{k\lambda}{D}\right) + 4\varepsilon\sin\theta \tag{9}$$

Relation 9 is the W–H equation and named uniform deformation model (UDM). In this model presumed that the strain is constant and monotonic in whole crystal geometric directions. so regarding the isotropic essence of the crystal and assuming that specifications of material are self-determining of the direction along that it is measured, the crystallite size D and strain ε can be estimated using the plot of 4sinθ (along the x-axis) vs. $\beta_{hkl}\cos\theta$ (along the y-axis) and by y-intercept and the slope of the linear fit, respectively [12]. Figure 3 indicates the plot of 4sinθ vs. $\beta_{hkl}\cos\theta$ for MNPs synthesized at different conditions. As shown, a positive and a negative slope in the plot indicate the presence of tensile strain in MgO-1 and MgO-2 samples (Fig. 3a, b) and compressive strain in MgO-3 nanoparticles (Fig. 3c).

The structural data for MgO nanopowders, including miller index, FWHM, diffraction angles, the crystallite size (using Scherrer's and W–H method), are reported in Table 1. The presence of compressive strains in MgO-3 nanoparticles can be attributed to supersaturating caused by the increase in NaOH concentration and the increase in particle interaction during the synthesis process.

The morphology of the MNPs synthesized from impure brine was analyzed by TEM and FESEM and is indicated in Fig. 4. Homogeneous distribution of nanoparticles with spherical morphology and smooth surfaces were observed in TEM and FESEM images. Characterization of the particle size distribution of the MgO nanopowders using Image-J software confirmed that the particle size range of MgO-1, MgO-2, and MgO-3 is 35–88 nm, 30–85, and 22–75 nm, respectively. It is evident from FESEM graphs that MgO-1 sample (Fig. 4a) has a better particle size distribution and more uniformity, while in MgO-2, and MgO-3 samples (Fig. 4b, c), with increasing NaOH concentration, the particles size have decreased and agglomeration increased (due to the increase of the specific surface area of MNPs). It should be noted that the average crystallite size calculated from XRD pattern is different from (less than) that of from FESEM technique. This confirms the polycrystalline quiddity of the MNPs.

EDS analysis is employed for the chemical analysis of MNPs that shown in Fig. 5. The EDS spectrum just indicated the existence of Magnesium (Mg), and Oxygen (O) elements in the samples, which proves the high purity of the synthesized powders. It is evident that the Mg/O atomic ratio, obtained from these results is in good match with that of the bulk ratio and corresponding XRD data. A slightly higher oxygen atomic ratio compared to that of magnesium is probably the absorption of moisture from the environment [13].

Figure 6 indicates the FTIR spectra of MNPs synthesized under various concentrations of the precipitator. For all samples, the same peaks are seen in FTIR patterns. The small peaks at 440, 510, and 880 cm^{-1} belong to the

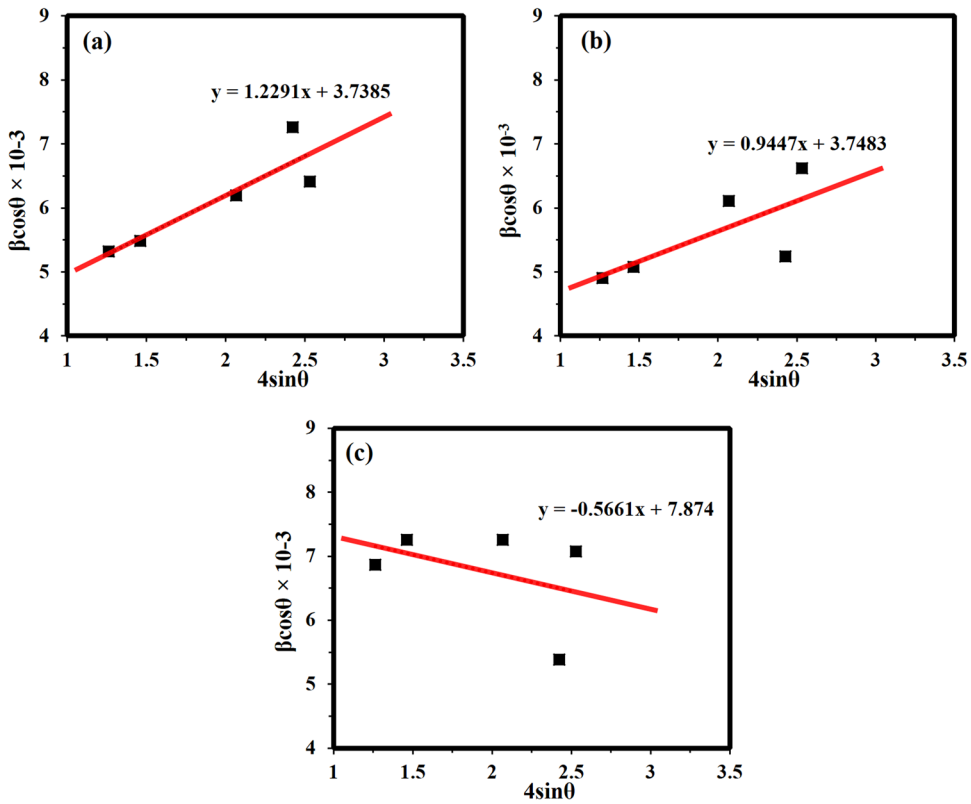

Fig. 3 W–H method and plots of 4sinθ vs $\beta_{hkl}\cos\theta$ for MNPs (UDM); **a** MgO-1 nanopowders, **b** MgO-2 nanopowders and **c** MgO-3 nanopowders

Table 1 Structural parameters for MgO-1, MgO-2, and MgO-3 nanoparticles

Sample	(hkl)	2θ	FWHM (degree)	D (Eq. 5) (nm)	W–H method	
					D	$\varepsilon \times 10^{-3}$
MgO-1	(111)	36.835	0.321	26.04	37.09	1.23
	(200)	42.847	0.337	25.29		
	(220)	62.221	0.414	22.37		
	(311)	74.549	0.523	19.09		
	(222)	78.510	0.474	21.60		
MgO-2	(111)	36.864	0.291	28.73	37.00	0.94
	(200)	42.831	0.378	22.54		
	(220)	62.208	0.423	21.95		
	(311)	74.567	0.633	15.77		
	(222)	78.517	0.514	19.95		
MgO-3	(111)	36.866	0.415	20.17	17.61	0.57
	(200)	42.845	0.446	19.09		
	(220)	62.219	0.486	19.09		
	(311)	74.573	0.388	25.72		
	(222)	78.437	0.523	19.58		

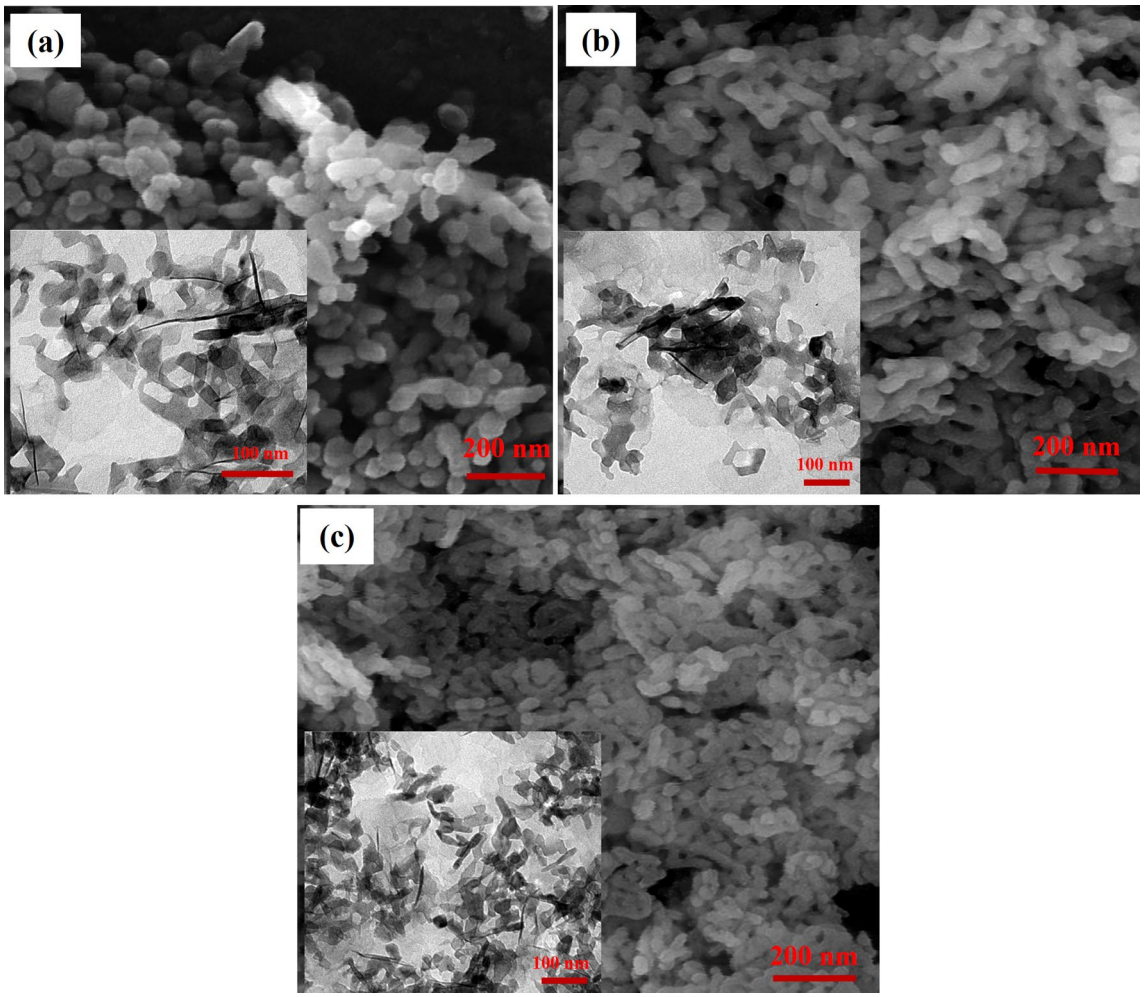

Fig. 4 FESEM and TEM (insert) images of synthesized MgO nanostructures by different concentration of NaOH, **a** 1 mol L^{-1}, **b** 2 mol L^{-1} and **c** 3 mol L^{-1}

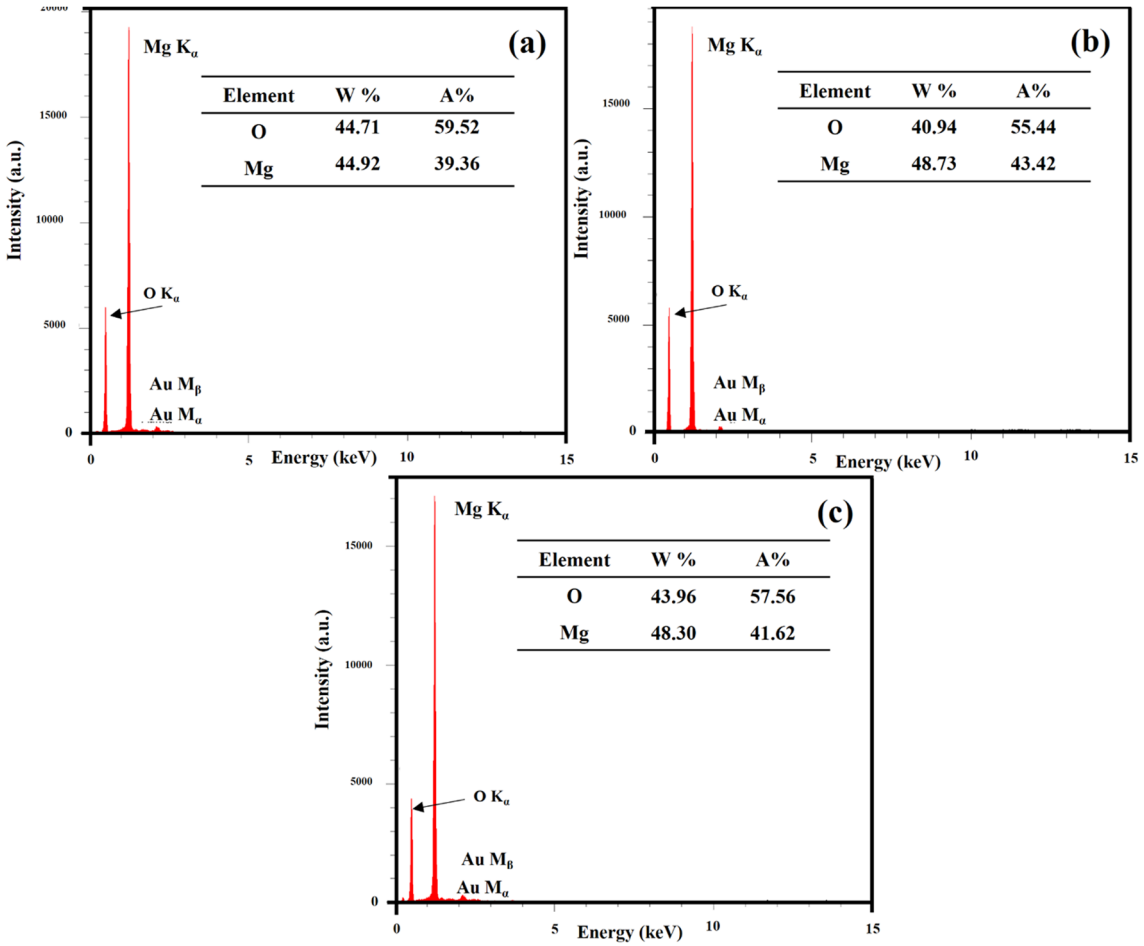

Fig. 5 FTIR spectra of the as-synthesized MNPs at different conditions

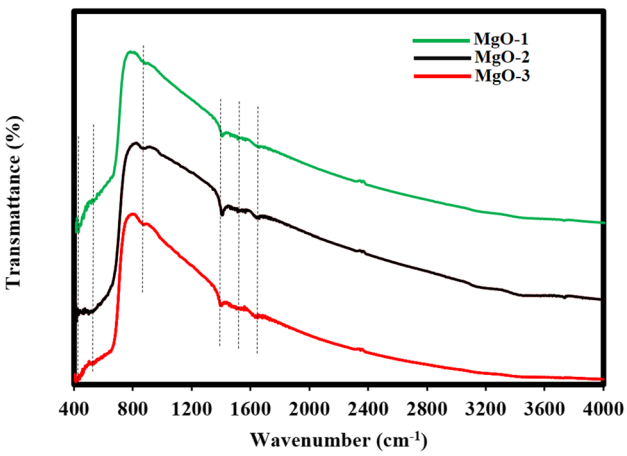

Fig. 6 FTIR spectra of the as-synthesized MNPs at different conditions

stretching vibration of Mg–O bands in MNPs [9, 14]. Also, the small peaks in ranges of 1400–1470 cm^{-1} are related to bending vibration of absorbed water and surface hydroxyl (–OH) from the atmosphere due to its surface acid–base properties [2, 15].

3.2 Optical properties

The optical properties of MNPs suspended in absolute ethanol was studied by UV–Vis spectroscopy. Figure 7a and b indicates the absorption and transmission spectra of the MNPs, respectively. According to Fig. 7a, the sharp and strong absorption peak at about 214 nm (MgO-1), 209 nm (MgO-2), and 211 nm (MgO-3) are due to the excitation of four-fold coordinated O^{2-} anions in the edges and corners that in agreement with the results obtained by other researchers [13, 15]. The higher absorption at the UV zone corresponds to the lower transmittance percent that is clear in Fig. 7b. In nanoscale, MNPs have a more sinificant percentage of atoms and defects on the surface than in bulk. These defects are located on the different coordination sites on the surface and undergo excitation when exposed to UV photon energy [13].

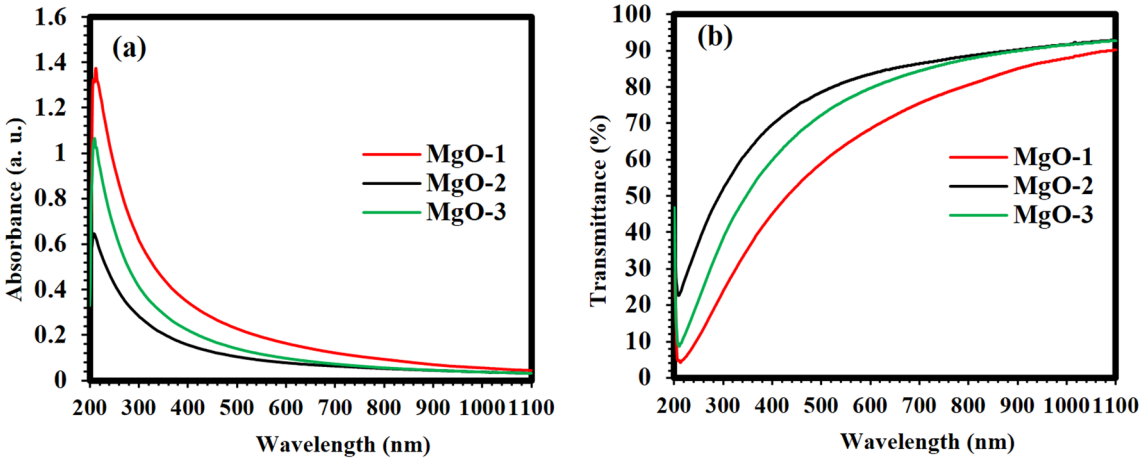

Fig. 7 Absorption **a** and transmittance (%) **b** spectra of as-synthesized MNPs

The relation between the 'α' (absorption coefficient) and the 'hν' (photon energy) can be specified by using Tauc's relation [16, 17]:

$$(\alpha h\nu) = A(Eg - h\nu)^n \tag{10}$$

where α, hυ, A, and E_g are the absorption coefficient, photon energy, material-dependent constant, and band gap energy, respectively, and 'n' is a constant related to the direct transition in semiconductors (equal to 0.5).

Also, the absorption coefficient of MNPs was calculated by the following formula [18]:

$$\alpha = 2.303\frac{A}{d} \tag{11}$$

where A and d are absorbance and the path length of the utilized quartz cuvette, respectively. The change in the 'α' as a function of the 'hυ' for as-synthesized MNPs are given in Fig. 8a. All samples show a high absorption coefficient in the UV zone, and this coefficient slakes in higher wavelengths.

To calculate the E_g for NPs, we used extrapolating the linear zone of the plot of $(\alpha h\nu)^2$ (x-axis) vs. hν (y-axis) that was determined by the x-intercept [7, 18] (Fig. 8b). The optical band gap energy value of the MgO-1, MgO-2, and MgO-3 was found to be 4.6, 4.7, and 4.9 eV, which shown the semiconducting manner of MNPs. Comparison of the XRD, FESEM results and measured E_g shown that the E_g had been increased by decreasing the size of nanoparticles (blue shift) (Fig. 9) and could be pertained to the electron confinement as perceived in past studies [8, 16, 18]. The E_g of MNPs was remarkably lower than the energy band gap from the standard value of Eg in the bulk state (7.8 eV) due to red-shifted from the standard. This was related to the

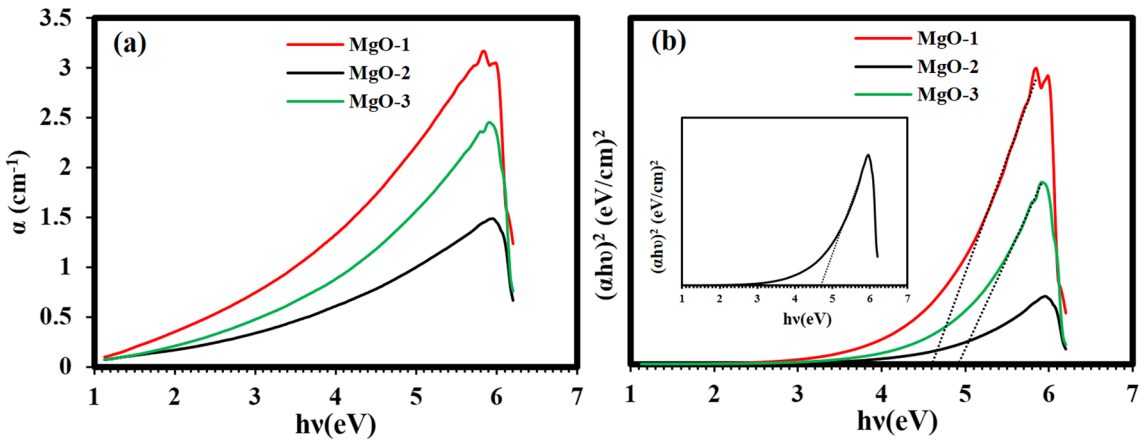

Fig. 8 **a** Variation of absorption coefficient with photon energy and **b** plot of $(\alpha h\nu)^2$ vs hν for MNPs synthesized by different concentrations of NaOH solution

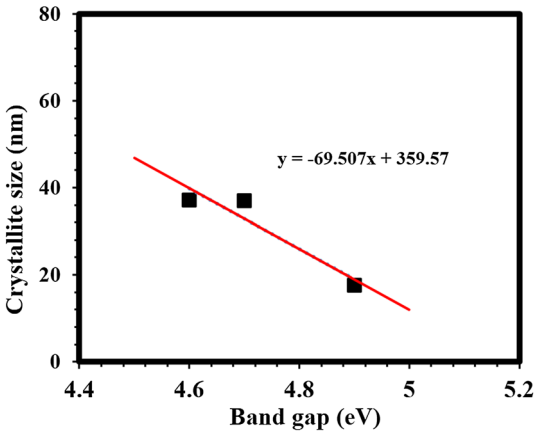

Fig. 9 Variation of the optical band gap energy with crystallite size in MNPs

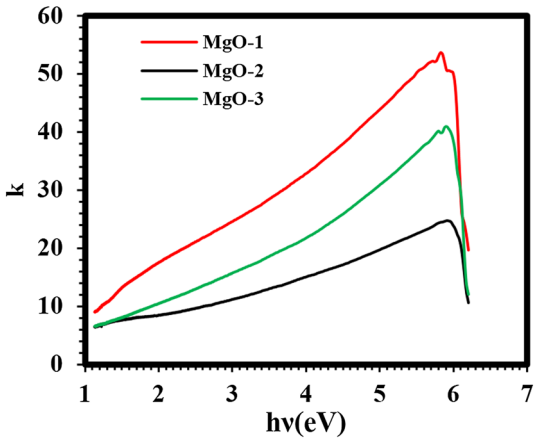

Fig. 10 The plot of extinction coefficient as a function of photon energy (eV) for MNPs

effect of the morphologies of crystals containing variant significant energetic facets, reaction of different excitation energy and so the creation of various direct band gaps and the quantum size effect [19, 20]. Also, these results were in good match with other previous works which used pure precursor for the synthesis of MgO nanostructures [1, 5, 21–24]. The synthesized MgO NPs from impure brine have geart potential in optoelectronics applications.

Extinction coefficient (k) affects various optical properties such as absorption of light waves in the medium and the dielectric constants. This parameter determines the part of light missed because of the dispersion and absorption per unit space of the infiltration environment [25]. The k value for MNPs samples was calculated by the following relation [26]:

$$k = \frac{\alpha\lambda}{2\pi} \tag{12}$$

where α and λ are the absorption coefficient and wavelength, respectively. Figure 10 exhibits the extinction coefficient of samples as a function of hv. Since the extinction coefficient and the absorption coefficient are proportional to each other, their variations are the same. As shown clearly, for MgO-1, MgO-2, and MgO-3 samples, the extinction coefficient increased gradually to 5.8 eV, 5.9 eV, and 5.9 eV, respectively, and then decreased. Increasing the extinction coefficient at low wavelengths (UV zone) was due to interactions between the photons and electrons, which affected the amplitude of the incident wave [27].

The refractive index (n) is a primary feature for all optical materials. It has a remarkable role in the study of optical materials, which is an important factor in optical information and medicine and surgery. This parameter is nearly dependent on the electronic polarization of ions and the localized field within these optical materials [28, 29].

Several simple formulas have been reported for relations among n and E_g in literature [30–33], which some of them have been investigated to certificate the current study. Based on Ravindra et al. [34], there is a linear relationship between the E_g and the high-frequency refractive index:

$$n = \alpha + \beta E_g \tag{13}$$

where α and β are equal to 4.048 and − 0.62 eV^{-1}, respectively. Herve and Vandamme [32] have suggested a tentative formula by simple utilization physics of light diffraction as:

$$n = \left(1 + \left(\frac{A}{E_g + B}\right)\right)^{1/2} \tag{14}$$

where A and B are constant and equal to 13.6 eV and 3.4 eV, respectively. Also, Gosh et al. [33] used various method by investigating the band structural and quantum-dielectric formulations of other researchers study as [35, 36]:

$$n^2 - 1 = \frac{A}{(E_g + B)^2} \tag{15}$$

where $A = 8.2E_g + 134$ (contribution of the valence electrons), $B = 0.225E_g + 2.25$ (constant additive to the lowest E_g), and $(E_g + B)$ is an adequate average energy gap of the material. So, these models were used to investigate the variation of n with the energy gap. Moreover, the estimated values of the optical dielectric constant (ε_∞) were attained using the relation $\varepsilon_\infty = n^2$ and Eqs. (13)–(16) [37, 38]. The estimated value for n and calculated ε_∞ for MNPs is listed in Table 2, indicating that Ravindra et al. model is an adequate model for MNPs and means high absorption

Table 2 Calculated refractive indices n for different MNPs using Ravindra et al. [33], Herve and Vandamme [31], and Ghosh et al. [32] models corresponding to optical dielectric constant ε_∞

Sample	E_g	n			ε_∞		
MgO-1	4.6	1.196[a]	1.972[b]	1.939[c]	1.430[a]	3.890[b]	3.762[c]
MgO-2	4.7	1.134[a]	1.954[b]	1.921[c]	1.286[a]	3.819[b]	3.691[c]
MgO-3	4.9	1.010[a]	1.919[b]	1.886[c]	1.020[a]	3.684[b]	3.557[c]

[a][31]
[b][29]
[c][30]

and low reflection may be related to developing in solar cell capability [7]. Also, the estimated n values for all three MgO nanopowders were lower than the bulk refractive index of MgO (1.74), which were in good match with other works [2, 7, 26].

4 Conclusions

MgO nanoparticles were prepared by a facile and economical method based on chemical precipitation from impure brine. XRD and EDS proved the formation of high purity single phase of MgO with FCC structure. According to the results of XRD and FESEM, increasing concentration of NaOH solution resulted in the reduction of the particle size of MNPs and increased their agglomeration. Due to decreasing particle size and quantum confinement effects, the optical properties of nanoparticles changed. One of these changes was the increase in the value of the optical band gap energy of MNPs from 4.6 to 4.9 eV. Our studies have shown that although MNPs were synthesized from impure brine, these nanoparticles exhibited excellent optical properties such as absorption, transmittance, band gap and refractive index, which could be used as submicron optoelectronic devices. Also, the Ravindra et al. model was an adequate model for MNPs according to obtained value n and ε_∞.

Acknowledgements The authors acknowledge the Semnan University and Dr Alireza Asghari (faculty of chemistry) for helpful assistances. Dedication to Sardare Delha (Q. Soleimani).

Compliance with ethical standards

Conflict of interest On behalf of all authors, the corresponding author states that there is no conflict of interest.

References

1. Zhao Y, Zhu G (2007) Synthesis of MgO microspheres with nanosheets in a mechanical force reactor and its optical property. Mater Sci Eng B 142:93–97
2. Hadia NMA, Mohamed HAH (2015) Characteristics and optical properties of MgO nanowires synthesized by solvothermal method. Mater Sci Semicond Process 29:238–244
3. Mbarki R, Hamzaoui AH, Mnif A (2015) Dielectric properties and electrical conductivity of MgO synthesized by chemical precipitation and sol-gel method. Eur Phys J Appl Phys 69:10402
4. Jeevanandam J, Chan YS, Danquah MK (2019) Effect of pH variations on morphological transformation of biosynthesized MgO nanoparticles. Par Sci Tech 38:1–19
5. Yousefi S, Ghasemi B, Tajally M, Asghari A (2017) Optical properties of MgO and Mg(OH)2 nanostructures synthesized by a chemical precipitation method using impure brine. J Alloys Compd 711:521–529
6. Al-Ghamdi AA, Al-Hazmi F, Alnowaiser F, Al-Tuwirqi RM, Al-Ghamdi AA, Alhartomy OA, El-Tantawy F, Yakuphanoglu F (2012) A new facile synthesis of ultra fine magnesium oxide nanowires and optical properties. J Electroceramics 29:198–203
7. Al-Gaashani R, Radiman S, Al-Douri Y, Tabet N, Daud AR (2012) Investigation of the optical properties of $Mg(OH)_2$ and MgO nanostructures obtained by microwave-assisted methods. J Alloys Compd 521:71–76
8. Obeid MM, Edrees SJ, Shukur MM (2018) Synthesis and characterization of pure and cobalt doped magnesium oxide nanoparticles: Insight from experimental and theoretical investigation. Superlattices Microstruct 122:124–139
9. Yousefi S, Ghasemi B (2019) Ultrasound-assisted synthesis of porous $Mg(OH)_2$ nanostructures using hypersaline brine. Micro Nano Lett 14:1019–1023
10. Navaladian S, Viswanathan B, Varadarajan TK, Viswanath RP (2009) A rapid synthesis of oriented palladium nanoparticles by UV irradiation. Nanoscale Res Lett 4:181–186
11. Rajesh Kumar B, Hymavathi B (2017) X-ray peak profile analysis of solid-state sintered alumina doped zinc oxide ceramics by Williamson-Hall and size-strain plot methods. J. Asian Ceram Soc 5:94–103
12. Bindu P, Thomas S (2014) Estimation of lattice strain in ZnO nanoparticles: X-ray peak profile analysis. J Theor Appl Phys 8:123–134
13. Salem JK, El-Nahhal IM, Hammad TM, Kuhn S, Sharekh SA, El-Askalani M, Hempelmann R (2015) Optical and fluorescence properties of MgO nanoparticles in micellar solution of hydroxyethyl laurdimonium chloride. Chem Phys 636:26–30

14. Yousefi S, Ghasemi B, Tajalli M, Asghari A (2018) Morphological and optical properties of magnesium hydroxide nanoplates synthesized by precipitation route. J Adv Mater Eng 36:59–67
15. Mageshwari K, Mali SS, Sathyamoorthy R, Patil PS (2013) Template-free synthesis of MgO nanoparticles for effective photocatalytic applications. Powder Technol 249:456–462
16. Al-Gaashani R, Radiman S, Tabet N, Razak Daud A (2019) Synthesis and optical properties of CuO nanostructures obtained via a novel thermal decomposition method. J Alloys Compd 509:8761–8769
17. Dar MA, Varshney D (2018) Structures and properties of $Mg_{0.95}Mn_{0.01}TM_{0.04}O$ (TM= Co, Ni, and Cu) nanoparticles synthesized by sol–gel auto combustion technique. RSC Adv 8:14120–14128
18. Al-Gaashani R, Radiman S, Daud AR, Tabet N, Al-Douri Y (2013) XPS and optical studies of different morphologies of ZnO nanostructures prepared by microwave methods. Ceram Int 39:2283–2292
19. Kato T, Okada G, Yanagida T (2016) Optical, scintillation and dosimeter properties of MgO translucent ceramic doped with Cr^{3+}. Opt Mater 54:134–138
20. Bindhu MR, Umadevi M, Kavin Micheal M, Arasu MV, Abdullah Al-Dhabi N (2016) Structural, morphological and optical properties of MgO nanoparticles for antibacterial applications. Mater Lett 166:19–22
21. Selvamani T, Yagyu T, Kawasaki S, Mukhopadhyay I (2010) Easy and effective synthesis of micrometer-sized rectangular MgO sheets with very high catalytic activity. Catal Commun 11:537–541
22. Dharshini MP, Sr GJ, Shally V, Manoharan D (2012) Variation of structural and optical parameters in transition metal oxide nanoparticles of Zn and Cu. Appl Res Dev Inst J 6:150–158
23. Wobbe MCC, Kerridge A, Zwijnenburg MA (2014) Optical excitation of MgO nanoparticles; a computational perspective. Phys Chem Chem Phys 16:22052–22061
24. Kumari L, Li WZ, Vannoy CH, Leblanc RM, Wang DZ (2009) Synthesis, characterization and optical properties of $Mg(OH)_2$ micro-/nanostructure and its conversion to MgO. Ceram Int 35:3355–3364
25. Hassanien AS (2016) Studies on dielectric properties, opto-electrical parameters and electronic polarizability of thermally evaporated amorphous $Cd_{50}S_{50}–xSe_x$ thin films. J Alloys Compd 671:566–578
26. Nemade KR, Waghuley SA (2014) Synthesis of MgO nanoparticles by solvent mixed spray pyrolysis technique for optical investigation. Int J Met 2014:1–4
27. Pavan Kumar CSS, Pandeeswari R, Jeyaprakash BG (2014) Structural, morphological and optical properties of spray deposited Mn-doped CeO_2 thin films. J Alloys Compd 602:180–186
28. Rathod PB, Waghuley SA (2016) Synthesis and Study of Optical Properties of Graphene/TiO2 Composites Using UV-VIS Spectroscopy. J Appl Spectrosc 83:586–591
29. Singh S (2002) Refractive index measurement and its applications. Phys Scr 65:167–180
30. Al-Douri Y, Khachai H, Khenata R (2015) Chalcogenides-based quantum dots: optical investigation using first-principles calculations. Mater Sci Semicond Process 39:276–282
31. Samara GA (1983) Temperature and pressure dependences of the dielectric constants of semiconductors. Phys Rev B 27:3494–3505
32. Hervé PJL, Vandamme LKJ (1995) Empirical temperature dependence of the refractive index of semiconductors. J Appl Phys 77:5476–5477
33. Ghosh DK, Samanta LK, Bhar GC (1984) A simple model for evaluation of refractive indices of some binary and ternary mixed crystals. Infrared Phys 24:43–47
34. Ravindra NM, Ganapathy P, Choi J (2007) Energy gap-refractive index relations in semiconductors - An overview. Infrared Phys Technol 50:21–29
35. Van Vechten JA (1969) Quantum dielectric theory of electronegativity in covalent systems. I. Electronic dielectric constant. Phys Rev 182:891–905
36. Penn DR (1962) Wave-number-dependent dielectric function of semiconductors. Phys Rev 128:2093–2097
37. Fakhri MA, Al-Douri Y, Bouhemadou A, Ameri M (2018) Structural and optical properties of nanophotonic $LiNbO_3$ under stirrer time effect. J Opt Commun 39:297–306
38. Abu Odeh A, Al-Douri Y, Ayub RM, Ibraheam AS (2016) Ultrasonic effect on optical, structural, topographical and morphological studies of Cu_2CdSnS_4 quaternary alloy nanostructures. J Alloys Compd 686:883–895